

Programming scheduled self-assembly of circadian materials

Received: 28 June 2024

Accepted: 17 December 2024

Published online: 02 January 2025

 Check for updates

Gregor Leech¹, Lauren Melcher^{2,8}, Michelle Chiu^{3,8}, Maya Nugent¹, Shirlaine Juliano¹, Lily Burton⁴, Janet Kang⁵, Soo Ji Kim⁴, Sourav Roy⁶, Leila Farhadi⁶, Jennifer L. Ross⁶, Moumita Das^{2,7}, Michael J. Rust⁵ & Rae M. Robertson-Anderson¹✉

Active biological molecules present a powerful, yet largely untapped, opportunity to impart autonomous regulation of materials. Because these systems can function robustly to regulate when and where chemical reactions occur, they have the ability to bring complex, life-like behavior to synthetic materials. Here, we achieve this design feat by using functionalized circadian clock proteins, KaiB and KaiC, to engineer time-dependent crosslinking of colloids. The resulting material self-assembles with programmable kinetics, producing macroscopic changes in material properties, via molecular assembly of KaiB-KaiC complexes. We show that colloid crosslinking depends strictly on the phosphorylation state of KaiC, with kinetics that are synced with KaiB-KaiC complexing. Our microscopic image analyses and computational models indicate that the stability of colloidal super-structures depends sensitively on the number of Kai complexes per colloid connection. Consistent with our model predictions, a high concentration stabilizes the material against dissolution after a robust self-assembly phase, while a low concentration allows for oscillatory material structure. This work introduces the concept of harnessing biological timers to control synthetic materials; and, more generally, opens the door to using protein-based reaction networks to endow synthetic systems with life-like functional properties.

The current state-of-the-art in next-generation materials design is to create structures that can achieve desired functions in response to external perturbations, such as self-repair in response to damage^{1–6}. Looking beyond this stimulus-response framework, we envision autonomously functional materials that can not only respond directly to their environment, but also have the capability to store a memory of past events and dynamically change their own properties^{7–11}. Such materials could be used to create dynamic sequestration devices that filter toxins on a programmable schedule, or medical implants that

self-assemble and restructure to protect and suture wounds and dissolve once fully healed.

An attractive strategy to equip materials with robust autonomous function is the use of distributed information processing throughout the material, rather than a central controller. This concept is similar to the function of interacting networks of biomolecules in living cells, which provide finely-tuned spatiotemporal regulation of physiology. In many cases, a small number of interacting network components can be isolated from the cell and retain modular function to achieve tasks

¹Department of Physics and Biophysics, University of San Diego, San Diego, CA, USA. ²School of Mathematical Sciences, Rochester Institute of Technology, Rochester, NY, USA. ³Graduate Program in Biophysical Sciences, University of Chicago, Chicago, IL, USA. ⁴Department of Biochemistry and Molecular Biophysics, University of Chicago, Chicago, IL, USA. ⁵Department of Molecular Genetics and Cell Biology and Department of Physics, University of Chicago, Chicago, IL, USA. ⁶Department of Physics, Syracuse University, Syracuse, NY, USA. ⁷School of Physics and Astronomy, Rochester Institute of Technology, Rochester, NY, USA. ⁸These authors contributed equally: Lauren Melcher, Michelle Chiu. ✉e-mail: randerson@sandiego.edu

such as defining structures with a specific size¹², generating spatial patterns¹³, or keeping time¹⁴. On a larger scale, the collective action of these biomolecules provides a way for energy flux to impart non-equilibrium properties into structures to create active matter. The last two decades have seen tremendous progress in identifying and understanding the emergent properties of active matter, from active colloids and molecular motor-driven active biomaterials, to soft robotics and living concrete^{15–23}. However, engineering autonomous materials with robust, kinetically-controlled activity, inherent to living systems, remains a grand challenge in materials science^{24–26}.

Here, we develop the proof-of-concept of an autonomous material with properties that are temporally programmed by biological signaling molecules using protein components derived from the cyanobacterial circadian clock (Fig. 1). In their natural context, KaiA, KaiB, and KaiC proteins generate a self-sustaining ~24-h rhythm that is used to synchronize physiology with the external light-dark cycle. Moreover, these proteins can be removed from their cellular context and can generate stable oscillations in a reconstituted *in vitro* system^{14,27–29}.

These oscillations can be detected as an ordered pattern of multisite phosphorylation on KaiC, which acts as a signaling hub that binds and releases protein partners throughout the cycle^{30–32}. In brief, KaiC consists of two tandem ATPase domains, CI and CII, arranged into a hexameric ring (one blue circle in Fig. 1A represents one subunit

consisting of a CI-CII pair). KaiA binds to the CII domain of KaiC, which stimulates autophosphorylation^{33,34}. Phosphorylation accumulates slowly throughout the day, first on Thr432, then on Ser431. When Ser431 is heavily phosphorylated (shown in Fig. 1D), corresponding to dusk, ring-ring stacking interactions allow the CII domain to regulate the slow ATPase cycle in CI³⁵. The post-hydrolysis state of CI allows KaiB to bind to KaiC³⁶ and six KaiB molecules to assemble cooperatively on the CI ring^{37,38}. KaiB is a metamorphic protein that is not competent to bind KaiC in its ground-state fold and must refold to form the KaiB–KaiC complex. Though ground-state KaiB can tetramerize, previous data suggests it is largely monomeric at standard concentrations^{37,39}.

This nighttime KaiB–KaiC complex sequesters and inactivates KaiA, closing a negative feedback loop to inhibit further phosphorylation and allowing KaiC to dephosphorylate. Unphosphorylated KaiC then releases KaiB and is ready to begin the cycle again. The kinetics of the phosphorylation rhythms are robust to temperature and protein concentration, yet can be tuned over a wide range by single amino acid substitutions in the Kai proteins^{40,41}. The system is also unusually thrifty in its energy consumption—with each KaiC molecule consuming only 15 ATP per day⁴². Thus, the Kai protein system is a uniquely attractive choice to develop into a synthetic tool to endow materials with programmable, autonomously time-dependent properties.

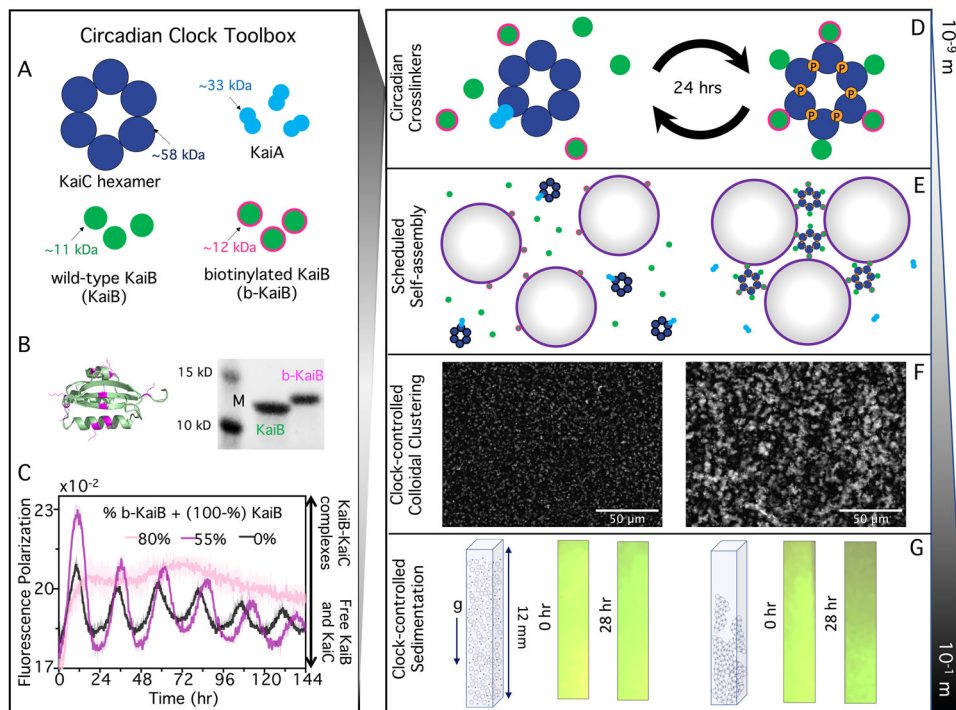


Fig. 1 | Harnessing circadian clocks to engineer non-equilibrium materials across scales. **A** We functionalize cyanobacteria clock proteins—hexameric KaiC rings (blue), KaiA dimers (cyan), and KaiB monomers (green)—to couple to materials by incorporating biotinylated KaiB (b-KaiB). **B** KaiB biotinylation: (left) example sites of possible amine-reactive biotinylation (magenta) overlaid on the KaiB crystal structure (green)^{60,61}, (right) SDS-PAGE gel of unlabeled KaiB and biotinylated KaiB (b-KaiB), showing successful biotinylation indicated by a mobility shift of the biotinylated product (molecular weight standards [M] are 10 and 15 kDa). **C** KaiABC reactions in the presence of biotinylated KaiB. Oscillations are measured by fluorescence polarization of FITC-labeled KaiB (0.2 μ M), a read-out of KaiB–KaiC complex formation. All conditions contain 3.5 μ M KaiB, with the specified fraction being b-KaiB. Oscillatory association of KaiB with KaiC is sustained with 55% b-KaiB (magenta), the percentage used in subsequent experiments, but not with 80% (pink). Each curve is the mean of two replicates. **D** KaiB monomers bind cooperatively to KaiC rings in a phosphorylation-dependent manner (indicated by the orange “P” circles), mediated by KaiA, and are subsequently released

as KaiC dephosphorylates over a 24-h cycle. We exploit the transition from free KaiB to KaiB fully assembled on a KaiC hexamer to create a time-dependent and phosphorylation-dependent change in crosslinking valency. **E** We incorporate the “circadian crosslinkers” depicted in **(D)** into suspensions of 1- μ m streptavidin-coated colloids to drive time-dependent crosslinking of colloids. **F** Microscope images of fluorescent streptavidin-coated colloids, mixed with KaiB, b-KaiB, and KaiC phosphorylation site mutants that cannot bind KaiB (left) or constitutively bind KaiB (right), show that KaiB–KaiC assembly selectively causes mesoscale clustering and connectivity of colloids. **G** Sedimentation of colloidal clock suspensions shown in **(F)** demonstrates pronounced settling of colloids after a day of incubation with the mutant that forms constitutively KaiB–KaiC complexes (right) compared to colloids mixed with the non-binding KaiC mutant (left). Cartoons depict the expected state of the suspension for constitutively binding (left) and non-binding (right) mutants (not drawn to scale). Source data for C are provided as a Source Data file.

Results and discussion

Biotinylation of KaiB allows KaiC to selectively mediate material crosslinking

To harness the Kai protein system for materials activation, we aimed to exploit the changing oligomeric state of KaiB, induced by interaction with KaiC, throughout the circadian cycle mediated by KaiA. Namely, KaiB transitions from being free in solution to forming a hexameric KaiB–KaiC complex (KaiBC). We reasoned that functionalized KaiB molecules would not be effective crosslinkers of material components when KaiB is free in solution, but that assembly into the KaiBC complex might create a potent multivalent crosslinker where time-dependent KaiB–KaiC interactions can bridge multiple biotin-streptavidin bonds (Fig. 1D). To develop this tool and characterize its effect, we chose a commercial colloidal suspension as a model material platform (Fig. 1E). We hypothesized that as KaiBC complexes form over time, the number of colloids able to participate in KaiB-mediated crosslinks would increase, and we would observe a transition from a fluid-like suspension of single colloids, to a gel-like state with larger connected clusters of colloids (Fig. 1E, F). Consistent with this prediction, we expect macroscopic changes in the ability of the colloidal material to sediment (Fig. 1G).

To endow the KaiBC complex with time-dependent material crosslinking properties, we first needed to functionalize KaiB to bind to the colloids strongly and statically, which we achieved through biotinylation of KaiB (Fig. 1A, B) and the use of streptavidin-coated colloids (Fig. 1E–G). We next needed to ensure that biotinylation of KaiB did not interfere with oscillatory assembly of the KaiBC complex (in the presence of KaiA), and that biotinylated KaiB (b-KaiB) could still bind to KaiC in a phosphorylation-dependent manner. To achieve the former, we used a fluorescence polarization (FP) assay to monitor rhythmic complex formation in the KaiABC reaction, finding that the reaction could tolerate the majority of the KaiB proteins being replaced by b-KaiB while still producing high amplitude rhythms (Fig. 1C). The altered amplitude of rhythms in the presence of b-KaiB may reflect a change in complex stability. In pull-down experiments, we found that b-KaiB retains its ability to interact with KaiC as well as its preference for the pS431 state (Fig. S1).

We next aimed to test the ability of KaiC to selectively crosslink b-KaiB-coated colloids via KaiBC complex assembly. To this end, we mixed b-KaiB into a suspension of 1- μm diameter streptavidin-coated colloids, then added either the pS KaiC mutant or the pT KaiC mutant to the suspension. pS and pT are mutated at the phosphorylation sites of KaiC to mimic either a state that permanently allows KaiB binding (pS–S431E;T432A, corresponding to the night phase) or prevents binding (pT–S431A;T432E, corresponding to the morning phase). By imaging the fluorescent-labeled colloids, we found that the colloids remained largely as isolated microspheres in the presence of the non-binding pT mutant, exhibiting no preferential self-association even after a day of incubation (Figs. 2A and S2).

This minimal self-association is similar to that observed without b-KaiB (Fig. S2), indicating that non-specific crosslinking is low. In contrast, Fig. 2B shows that b-KaiB-coated colloids incubated with the binding-competent pS KaiC mutant grow into large colloidal aggregates. This crosslinking mechanism is robust, producing qualitatively similar effects with different-sized colloids (Fig. 2C, D), and forming structures that are system-spanning and relatively immobile compared to pT KaiC samples in all cases (Fig. S3). Thus, b-KaiB can act as a potent material crosslinker that functions only in the presence of appropriately phosphorylated KaiC.

To demonstrate that these mesoscopic structural changes can translate to macroscopic material changes visible to the naked eye, we imaged colloidal suspensions undergoing sedimentation in capillaries on the centimeter scale over the course of a day. We observed macroscopic sedimentation dependent on the phosphorylation of KaiC: the larger microscopic clustering seen for pS is mirrored by

pronounced sedimentation of the suspension, while the pT colloids remain suspended (Fig. 2E).

To further establish the robustness and specificity of this self-assembly process, we performed experiments in which we: (1) removed KaiC (Fig. 2F), (2) removed b-KaiB (replacing with wild-type KaiB) (Fig. S2), and (3) replaced streptavidin-coated colloids with passivated non-functionalized colloids (Fig. S4). We observed no clustering in any of these control experiments (Fig. S5). We also performed experiments in which we replaced Kai proteins with bovine serum albumin (BSA) or PEG polymers that have multiple biotinylation sites, but are present on the same linker molecule rather than brought together by macromolecular complex assembly, as in the Kai protein system. While, in principle, these polymer linkers have the potential to act as crosslinkers to bind streptavidin-coated colloids, we found minimal clustering for all linker sizes and number of biotin sites (Figs. 2G and S6). Thus, the self-assembled structures we observe specifically require the formation of KaiBC complexes. We understand this unique feature as arising from the fact that KaiC acts as a “middle-man” to crosslink colloids via binding to b-KaiB. In this way, all biotin moieties on a single b-KaiB can be bound to the same colloid without preventing KaiC association. In the alternative designs, all biotin moieties that could crosslink two colloids are on the same construct, which strongly favors their binding to the same colloid over a neighboring one. This unique selectivity is an important functional feature of the KaiABC crosslinking system, independent of its potential for oscillatory behavior.

Crosslinking proceeds with kinetics programmed by clock proteins

To characterize the clock-driven clustering kinetics that program the colloidal suspensions to transition from freely floating particles to large, connected superstructures, we collected images of the emerging clusters at nine different time points over the course of a day. To promote mixing and limit colloid settling and surface adsorption, we kept all samples under continuous rotation between imaging intervals. Overlaying temporally color-coded images from these time-course experiments confirms that structure emerges over time in the pS KaiC sample, while minimal clustering is seen in the presence of pT (Fig. 3A, B).

To quantify the time-dependent colloidal self-assembly that is apparent in microscopy images, we use spatial image autocorrelation (SIA) analysis to measure the average size of colloidal clusters at each time point. SIA quantifies the correlation $g(r)$ between pixels separated by a radial distance r (Figs. 3C and S7), which decays exponentially from $g(0) = 1$ with the decay rate indicating the characteristic size of features in an image. Slower decay of $g(r)$ with r indicates larger features (i.e., clusters), as seen for pS compared to pT and long compared to short times (Figs. 3C and S7). By fitting each $g(r)$ curve to an exponential decay, we quantify a characteristic correlation lengthscale ξ of the colloidal system, indicated by the distance r at which the dashed horizontal line intersects each curve in Fig. 2C. We also implemented alternative image analysis algorithms to assess clustering, including quantifying the distribution of pixel intensities (Figs. 3D, E and S7) and directly detecting clusters as connected regions in a binarized image (Figs. S7 and S8), both yielding similar results to SIA (Figs. 3D, E, S7 and S8). Specifically, the full pixel intensity distribution width at 1% (FW1%) and median cluster size both display similar time-dependence as ξ (Fig. 3F). To directly compare these different clustering metrics, we normalize each quantity by the corresponding initial value for pT such that the values indicate the degree of clustering, which is one in the absence of clusters (Fig. 3F).

Given that pS KaiC is locked into a binding-competent state, the gradual self-assembly of colloids over many hours, suggests that the rate-limiting step in self-assembly is KaiB–KaiC complex formation rather than the time needed for colloids to come into close contact. Indeed, KaiBC complexes are known to form on the timescale of many hours, likely due to both the slow ATPase cycle in the KaiC CI domain⁴³

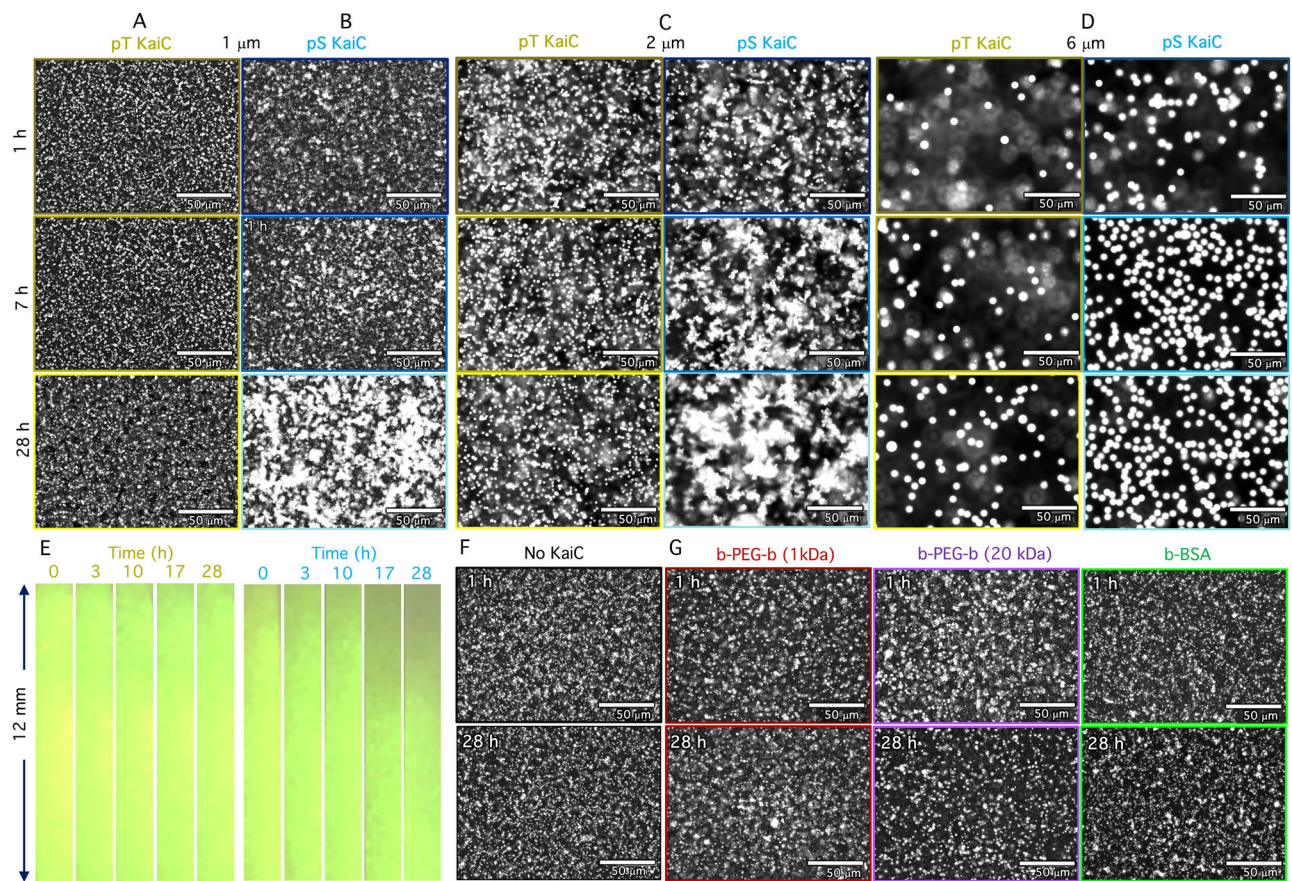


Fig. 2 | KaiB–KaiC complexes crosslink colloids with high specificity in a phosphorylation-dependent manner. Fluorescence microscopy images of suspensions of 1- μm diameter colloids taken at 1 h (top), 7 h (middle), and 28 h (bottom) after mixing with KaiC mutants that are frozen in **A** non-binding (pT) or **B** binding (pS) states show substantial clustering and assembly of pS-colloids over time that is absent for pT-colloids. Fluorescence microscopy images of suspensions of colloids of 2 μm (**C**) and 6 μm (**D**) diameter in the presence of pT and pS KaiC proteins show that timed aggregation, dependent on the phosphorylation state of KaiC, is preserved for different sizes of colloids. The concentrations of colloids, proteins, and reagents, as well as imaging parameters, are identical to those in (**A**, **B**). **E** Images of a suspension of 1- μm diameter colloids undergoing sedimentation in a 12 mm long capillary over 28 h in the presence of pT (left) and pS (right) show that pS-colloids sediment more quickly, as indicated by dark regions

extending further down the images. The time that each image is captured is listed at the top. **F** The same suspension parameters as in (**A**, **B**) but without KaiC (including only KaiB and b-KaiB) show minimal clustering over the course of 1 h (top) to 28 h (bottom), demonstrating that the KaiB–KaiC complex formation is essential to the colloidal self-assembly shown in (**A**–**E**). **G** Suspensions of streptavidin-coated colloids, with identical conditions to those in (**A**, **B**), but with Kai proteins replaced with alternative biotinylated constructs that could, in principle, crosslink streptavidin-coated colloids: (left) 1 kDa biotin-PEG-biotin with 1 biotin on each end, (middle) 20 kDa biotin-PEG-biotin with 1 biotin on each end, and (right) biotin-BSA with 8–16 biotins. The molarity of PEG and BSA matched the KaiC molarity used in (**A**–**E**), and minimal clustering is observed from 1 h (top) to 28 h (bottom), demonstrating that the effect shown in (**A**–**F**) is unique to the KaiB–KaiC binding interaction.

and the time required for KaiB to refold into an alternative fold-switched structure^{39,44}. To test this hypothesis, we measured the kinetics of the KaiBC interaction using FP of labeled KaiB, which increases with increasing formation of KaiBC complexes, and compared the results to the kinetics of material self-assembly. Figure 3F shows in overlay the time evolution of the relative FP, demonstrating that KaiBC complex formation grows approximately linearly for the first 15 h after which it approaches saturation, likely reflecting a regime where the majority of both KaiB and KaiC molecules are in complex and have been depleted from solution. The agreement between the kinetics of KaiBC interactions and material self-assembly shown in Fig. 3F, as well as the robust specificity of the colloidal assembly (Fig. 2A, B, F), is strong evidence that the biochemical properties of the Kai proteins, such as the KaiC catalytic cycle, are regulating the rate of cluster growth.

Brownian Dynamics simulations recapitulate timing of cluster formation

The correlation of KaiB fluorescence polarization with the clustering of colloids suggests that Kai protein interactions control the kinetics of

clustering. In order to assess this mechanism, we developed a numerical simulation that captures the key components of our experimental system (see section “Methods” and SI). In the simulations, 1- μm diameter colloids move via Brownian motion in a 50 μm \times 50 μm 2D plane, and, when the surfaces of two colloids are within 10 nm of each other (comparable to the size of the KaiBC complex⁴⁵), they can form a bond mediated by b-KaiBC complexes. KaiB and KaiC are assumed to be present at constant concentrations and their interaction to form crosslinks is treated phenomenologically. The probability of complex formation during an encounter is a constant value chosen to match the solution-binding kinetics (see SI). We allow simulations to run for 30 h and capture the state of the colloids at the same time intervals as in experiments (Fig. 4).

To model our experimental pS KaiC and pT KaiC colloidal systems, we consider cases in which, respectively, bonds between colloids are incapable of releasing once they are formed (Fig. 4B) and bond formation probability is zero (Fig. 4D). The color-coded temporal overlays of simulation images with “permanent bonds” (*P*) and “no bonds” (*N*) show qualitative similarities with the experimental overlays

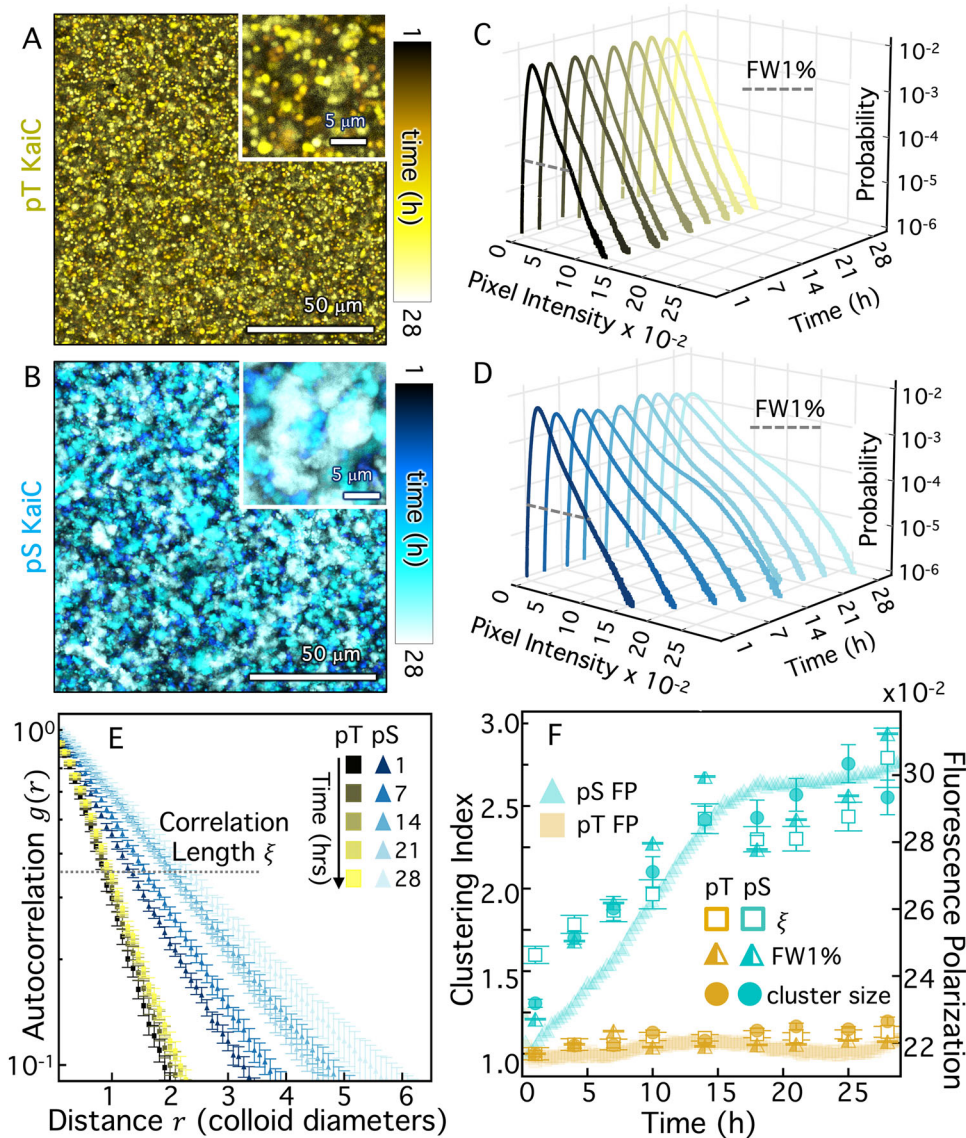


Fig. 3 | KaiBC crosslinking mediates robustly timed self-assembly of colloidal clusters that are synced with KaiBC complex formation. Colorized temporal projections of time-lapses of pT KaiC (A, yellow) and pS KaiC (B, cyan) over the course of 28 h, with colors indicating increasing time from dark to light according to the color scales. (Insets) Zoomed-in regions of the projections highlighting pS-specific cluster growth over time that is absent for pT. Pixel intensity probability distributions for pT (C, yellow), and pS (D, cyan) at different times over 28 h, with lighter shades denoting later times according to the color scales in (A, B). Distributions show broadening and emergence of high-intensity peaks at later times for pS. Dashed gray line denotes the full width at 1% of the maximum probability (FW1%), which serves as a clustering metric used in (F). Data are generated from the same images used to generate colormaps in (A, B). E Spatial image autocorrelation functions $g(r)$ versus radial distance r (in units of colloid diameter) for 5 different times between 1 and 28 h for pT (yellow) and pS (cyan) with color shade indicating

time according to the legends in (A, B). The characteristic correlation length ξ , determined by fitting each $g(r)$ curve to an exponential function, is denoted by the intersection of the dashed horizontal line at $g = e^{-1}$. Data shown are the mean and SEM across 36 images from two replicates. F Correlation lengths ξ (open squares), FW1% (half-filled triangles), and median cluster size (filled circles, see Figs. S7 and S8), each normalized by their initial pT value, show that the time course of cluster assembly over 28 h for pT (gold) and pS (cyan) correlate with the fluorescence polarization (FP) of fluorescently labeled KaiB (right axis, mP), which serves as a proxy for KaiBC complex formation. Both the degree of clustering and FP remain at a minimum for pT, while for pS, both steadily increase for the first -15 h. ξ , FW1%, and cluster size data are the mean and SEM across 36 images from two replicates. FP data are the mean and SEM (too small to see) of three replicates. Source data are provided as a Source Data file.

of pS and pT (Fig. 4C, E). To quantitatively compare simulated and experimental cluster assembly kinetics, we perform the same SIA analysis that we use for experimental images (Fig. 3C) to compute time-dependent autocorrelation curves (Fig. 4F) and corresponding correlation lengths (Fig. 4G). Similar to the $g(r)$ trends we observe for experimental pT and pS images (Fig. 3C), Fig. 4F shows that $g(r)$ for the “no bonds” system exhibits minimal time-dependence and fast decay with distance r , indicative of small features that do not change size over time. Conversely, $g(r)$ for the “permanent bonds” case (P) decays

more slowly than N at all time points and broadens substantially over time, indicative of larger clusters that grow over time. The time course of the corresponding correlation lengths of the 30-h simulation are similar to the experimental trends shown in Fig. 3F, with ξ values for P growing over time and transitioning to slower increase in the latter half of the simulation.

The continued cluster growth for pS (experiments) and P (simulations) is somewhat unexpected given the saturation of the fluorescence polarization at -15 h. Specifically, FP saturation suggests

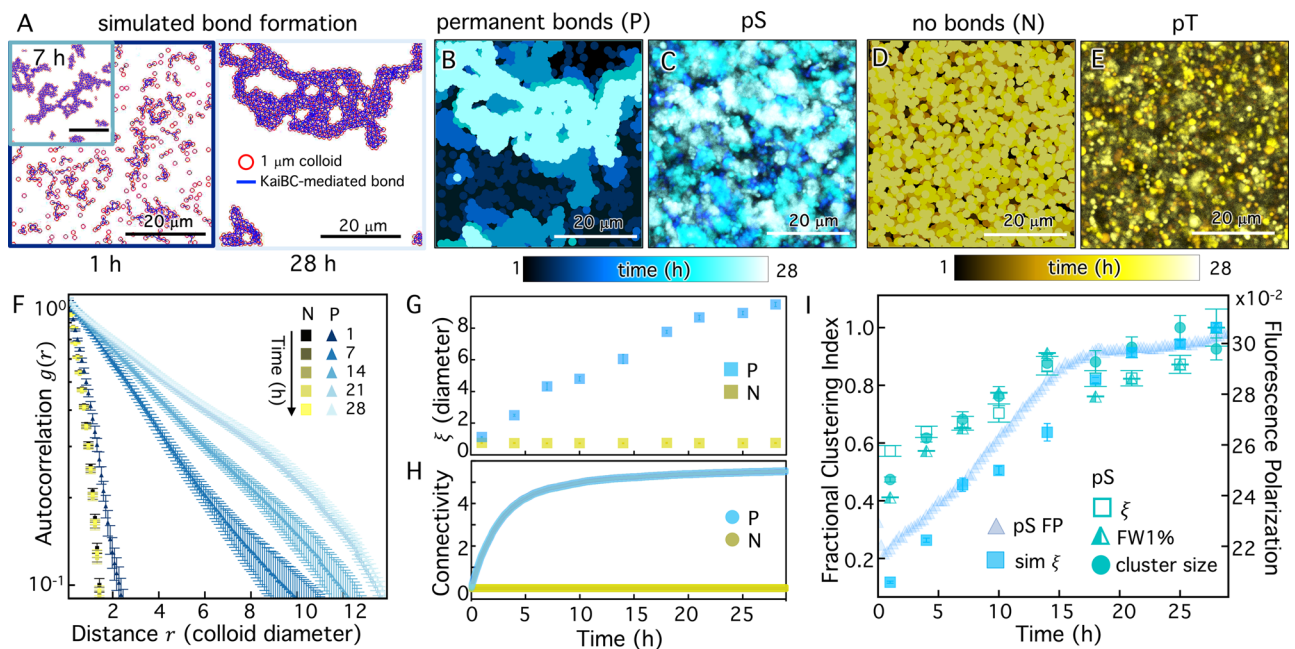


Fig. 4 | Kinetic simulations of Kai-mediated crosslinking recapitulate slow formation of colloidal clusters. **A** Simulation snapshots showing clustering of colloids (red circles) crosslinked by permanent bonds (blue lines), analogous to the experimental pS-colloid system, at 1 (left), 7 (inset), and 28 (right) hours. Colorized temporal projections of **(B)** simulation snapshots for colloids with permanent crosslinker bonds (permanent bonds, P) and **(C)** experimental snapshots for pS-colloids show similar features emerging over the course of a day. Colorized temporal projections of **(D)** simulation snapshots for colloids with no crosslinker bonds (no bonds, N) and **(E)** experimental snapshots for pT colloids both show minimal clustering or restructuring over the course of a day. Times and color-coding used in projections are the same as in Fig. 3, as indicated by the color scales. **F** $g(r)$ computed for simulation snapshots, taken at times specified in the legend, for colloids with no bonds (N, yellow squares) and permanent bonds (P, cyan triangles). Time

course of the **(G)** correlation lengths ξ and **(H)** colloid connectivity number CCN determined from simulations with permanent bonds (P, cyan) and no bonds (N, gold). **I** Multiple metrics of clustering and self-assembly resulting from permanent crosslinker bonding in experiments (pS) and simulations (P), each normalized by its maximum value to indicate the fractional clustering index (left axis) measured using each metric. Metrics include: experimental correlation lengths (ξ , open squares), simulated correlation lengths (sim ξ , filled squares), full width at 1% (FW1%, half-filled triangles), and median cluster size (cluster size, filled circles). Trends in both simulation and experimental data track with the time course of KaiB fluorescence polarization (right axis (mP), translucent triangles) in a reaction with pS KaiC. All simulation data shown is the mean and SEM across five replicates. Experimental data shown in **(C, D, I)** are reproduced from Fig. 3. Source data are provided as a Source Data file.

that all possible KaiBC complexes have formed, while the colloid data suggest that clusters continue to form and grow after this saturation. To shed light on this seeming paradox, we compute the colloid connectivity number (CCN) from simulations, which measures how many neighboring colloids are connected to a single colloid. Because of the 2D geometry and the size of the colloids, the maximum possible CCN is six. Figure 4I shows that CCN increases to saturating levels over the course of ~10–15 h, similar to the KaiBC FP data, while the simulated correlation lengths continue to increase after this time, albeit less dramatically than the first half of the time course (Fig. 4G). These data indicate that cluster growth can proceed even when the majority of colloids are saturated with permanent crosslinks. Such assembly kinetics may arise if the majority of saturated colloids are in the interiors of clusters, while those on the boundaries have available b-KaiB binding sites to crosslink to other colloids on the edges of neighboring clusters. Self-assembly thus transitions from that of single colloids coming together to form clusters, to one in which most colloids are participating in clusters that then merge to form larger superstructures. Figure 4I corroborates this physical picture by comparing the kinetics of cluster formation in the experimental and simulation data with the KaiBC assembly kinetics. The similarity in the shapes of the experimental and simulation curves indicates that the model is indeed capturing the underlying process of generating clusters. The clear shift in kinetics at ~15 h in all data further corroborates the robustness of the simulations, and demonstrates that self-assembly is rate-limited by the timescale of KaiBC complex formation.

Oscillations in colloidal clustering depend on the crosslinker density

Having demonstrated that material self-assembly can be temporally programmed by the phosphorylation state of the circadian clock proteins, we now investigate the effect of oscillatory interactions between KaiB and KaiC in the wild-type system when KaiA is present. To achieve oscillatory crosslinking, we replace the phosphorylation-locked mutants with wild-type (WT) KaiC and add KaiA, creating a circadian rhythm in both KaiC phosphorylation (mediated by KaiA) and the KaiB–KaiC interaction (Fig. 1C, D).

To guide our experiments, we first aimed to understand how oscillating crosslinkers may translate to the dynamics of material self-assembly. To do so, we extended our model shown in Fig. 4 to allow sinusoidally varying colloid binding and unbinding rates (see section “Methods”, SI). In brief, we consider the same binding rate amplitude p_o as in the permanent bond case but we incorporate an oscillation of this rate, $p_{on} = p_o \cos^2(\pi t/T)$, where T is the oscillation period. This construction models the coherent bulk oscillations in the biochemical properties of the KaiABC reaction. We also add a dissociation rate with the same amplitude and functional form as the binding rate, but that is $\pi/2$ radians out of phase, i.e., $p_d = p_o \sin^2(\pi t/T)$. This framework assumes that each connection between two colloids is bonded by a single KaiBC complex ($n = 1$). Figure 5A shows that this minimal bonding allows for oscillatory connectivity, with peaks in CCN observed at times that are in phase with the peaks in the input oscillatory binding and that roughly correlate with the measured peaks in KaiC phosphorylation (Figs. 5D and S9). However, the peak CCN values

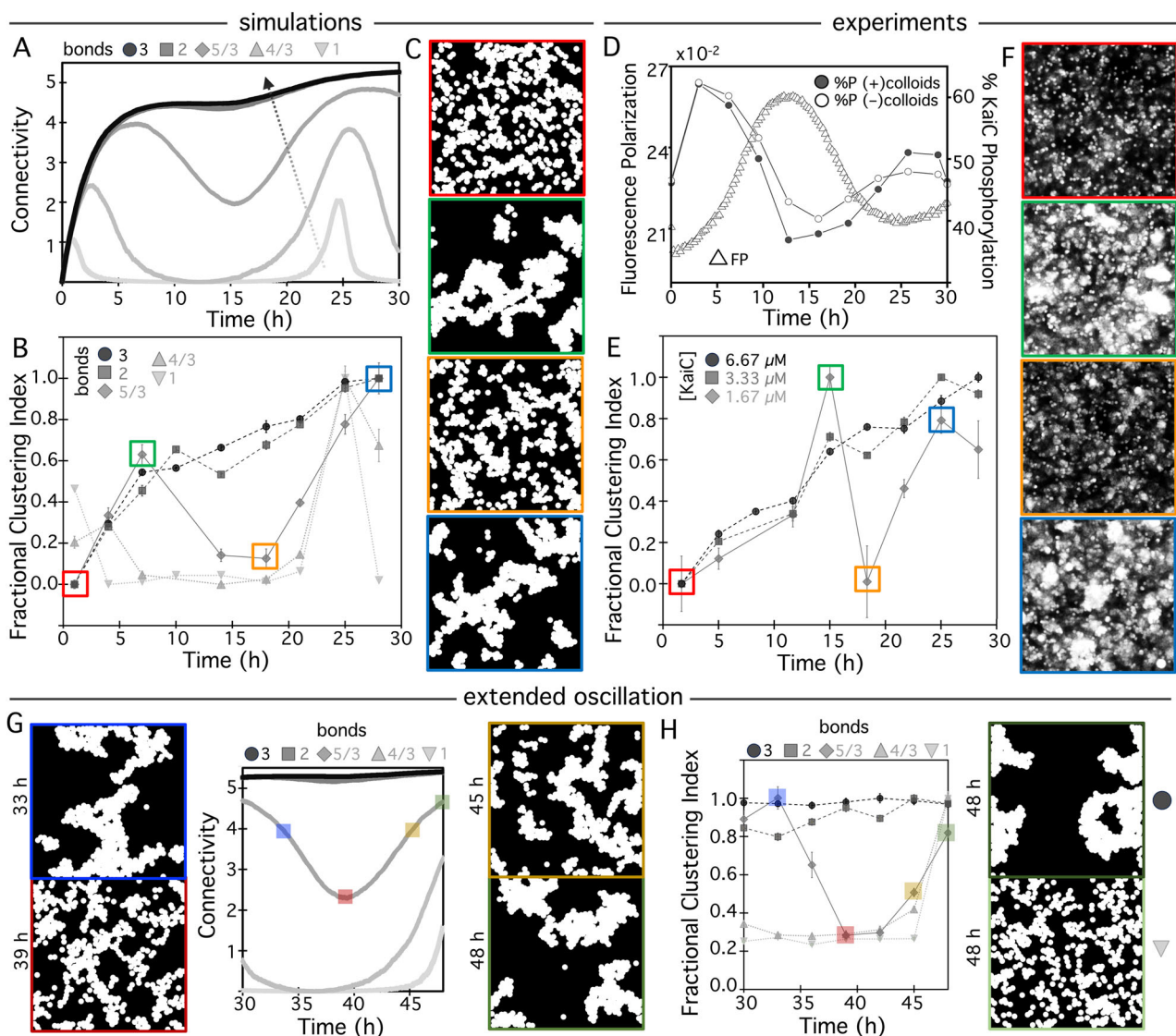


Fig. 5 | Oscillatory material properties depend on crosslinker density.

A–C Simulations model oscillatory colloidal crosslinkers with different numbers of KaiB–KaiC complexes (n , bonds) participating in each connection between colloids. **A** Colloid connectivity (CCN) versus time for systems with different numbers of bonds per colloid connection, from light to dark gray: $n = 1, 4/3, 5/3, 2, 3$. Arrow indicates direction of increasing n . Intermediate bond numbers $1 < n < 2$ result in oscillating connectivity, while $n = 1$ is not sufficient for pronounced clustering and $n \geq 2$ promotes sustained cluster growth with minimal dissolution. **B** The fractional clustering index (see text) versus time for bond densities shown in **(A)** reveal oscillatory clustering for $n < 2$ that is most pronounced for $n = 5/3$. The colored boxes enclose the data points corresponding to the simulation images with color-matched borders shown in **(C)**. **C** Simulation snapshots that correspond to troughs (red, orange) and peaks (green, blue) shown in **(B)** demonstrate that peaks and troughs correspond to substantial and minimal clustering, respectively. **D** Fluorescence polarization (FP) of KaiB (left axis, triangles) and percentage of phosphorylated KaiCs (%P, right axis, circles) during a KaiB–KaiC reaction. %P measurements were performed in the presence (filled circles) and absence (open circles) of colloids, showing that oscillatory KaiC phosphorylation dynamics are unaffected by the presence of colloids (see Fig. S9). **E, F** The fractional clustering

index versus time for colloid experiments performed with KaiC concentrations of $6.67 \mu\text{M}$ ($1\times$, dark gray circles), $3.33 \mu\text{M}$ ($0.5\times$, gray squares), and $1.67 \mu\text{M}$ ($0.25\times$, light gray diamonds) reveal oscillatory clustering for the lowest concentration, similar to the simulated $n = 5/3$ case, while the two higher concentrations steadily become increasingly clustered over time, similar to the simulated $n \geq 2$ cases. Colored boxes enclose the data points corresponding to the microscope images with color-matched borders shown in **(F)**. **F** Microscope images that correspond to troughs (red, orange) and peaks (green, blue) shown in **(E)** show strong similarities to simulated images and demonstrate minimal and substantial clustering, respectively. Simulated colloid connectivity **(G)** and fractional clustering index **(H)** for extended times (30–48 h) for the same bond numbers examined in **(A–C)**. Simulation snapshots are shown for the $n = 5/3$ case at 33 (blue), 39 (red), 45 (brown), and 48 (green) hours, as well as the $n = 1$ and $n = 3$ cases at 48 h (right column). Translucent boxes that match the snapshot borders indicate the corresponding connectivity and fractional clustering index. All simulated and experimental images shown are $50 \mu\text{m} \times 50 \mu\text{m}$. All experimental data shown is the mean and SEM across 36 images from two replicates. All simulation data shown is the mean and SEM across five replicates. Source data are provided as a Source Data file.

are low compared to the saturating value of 6, and non-zero CCN values are only maintained for a small fraction of the oscillation period, suggesting very weak oscillatory clustering.

However, given the saturating level of Kai proteins in our experiments ($\sim 10^5$ b-KaiB proteins per colloid) and the two orders of magnitude smaller size of the crosslinkers compared to the colloid

surface area, we anticipate that more than one KaiBC bond participates in a typical connection between two colloids in experiments. To incorporate multiple bonds per connection into our simulations we modify the dissociation rate to include the number n of bonds that participate in each colloid connection, as $p_d = p_d^0 \sin^2(\pi n/T)$. Additional curves in Fig. 5A show that $n = 2$ and $n = 3$ produce saturating

connections that are unable to appreciably dissociate during a bond oscillation cycle. However, for intermediate cases $n = 4/3$ and $5/3$, we observe pronounced oscillations in connectivity, suggesting similar oscillatory clustering of colloids.

Similar to Fig. 4, we translate connectivity to clustering kinetics by computing the correlation length for each time point that is captured in experiments. To compare the time dependence of complex formation for different bond numbers we evaluate the fractional clustering index, which we define as the baseline-subtracted correlation length, $\xi(t) - \xi_{\min}$, normalized by the corresponding maximum value, $\xi_{\max} - \xi_{\min}$: $FCL = (\xi(t) - \xi_{\min}) / (\xi_{\max} - \xi_{\min})$. All values of this function lie between 0 and 1 to allow us to isolate the time dependence of the clustering. Figure 5B shows that robust oscillatory clustering is achieved for $n = 4/3$ and $5/3$, with the initial peak being more pronounced for $n = 5/3$. Figure 5C shows the simulation snapshots that correlate with the peaks and troughs of the clustering index, visually demonstrating the presence of large superstructures at the peaks and minimal clustering at the troughs.

We understand this complex dependence on bond density as follows: a low density of crosslinkers (i.e., $n = 1$) does not allow superstructures to form, simply because many particles will not be able to find an attachment point, even if the Kai proteins in the system are in a binding-competent state. However, at high crosslinker density (i.e., $n \geq 2$), multivalent effects prevent superstructures from easily disassembling once formed, even when the KaiBC binding probability falls. Thus, the model predicts a “sweet spot” in crosslinker density (i.e., $1 < n < 2$) where the underlying molecular rhythm in KaiBC interaction will be transduced into material properties with high amplitude (Fig. 5B, C).

Armed with these predictions, we performed experiments at different Kai concentrations, to mimic varying n values in simulations. We first aimed to demonstrate that the ~24 h oscillation in KaiBC complex formation is not disrupted by the presence of colloids. Figure 5D confirms that the expected oscillation in KaiBC complex formation, measured by FP, is unperturbed by the buffer conditions used for assembling colloidal materials; and that the oscillatory phosphorylation of KaiC is similarly preserved (Fig. S9) and largely unaffected by the presence of streptavidin-coated colloids.

We then performed the same full time course of microscopy measurements as for the pS and pT mutants (Fig. 2) at $1\times$, $0.5\times$, and $0.25\times$ of the Kai concentration used in the mutant experiments ($6.66\ \mu\text{M}$, Figs. 2 and 3). Evaluating the same fractional clustering index as in simulations (Fig. 5B), we find that for the two higher concentrations, colloid superstructures assemble slowly over the course of the day, but show no detectable disassembly, similar to the $n \geq 2$ simulations (Fig. 5B, E). However, at the lower Kai concentration ($0.25\times$, $1.67\ \mu\text{M}$), oscillatory clustering appears (Fig. 5E, F), with peak and trough times corresponding approximately to the peak and trough KaiBC interaction detected by FP (Fig. 5D). The clustering, dissolution and re-clustering quantified by the fractional clustering index (Fig. 5E) can be observed in the corresponding microscope images (Fig. 5F) which have very similar features to the simulated images (Fig. 5C).

These results demonstrate the achievement of timed assembly and disassembly of a material and the power of predictive modeling to identify the appropriate region of phase space to achieve this engineering feat. To further demonstrate the oscillatory nature of the assembly, we extend the timescale of simulations out to 48 h over which we expect to capture an additional assembly oscillation. As shown in Fig. 5G, H, we observe a similar oscillation in connectivity and clustering index as in the first 24 h, with similar dependence on n . Simulation snapshots at the peaks and trough of the oscillations are also highly similar to those shown in Fig. 5C, demonstrating repeatable oscillatory assembly and disassembly.

While oscillatory material assembly indeed represents a transformative advance in materials design, we also point out that the

robust time constant associated with the material assembly, dictated by KaiBC complex formation, provides an additional important technological advance. Indeed, the kinetics of cluster assembly are robustly regulated, nearly independent of protein concentration, when we use non-oscillating mutants to program the assembly phase of the material (Fig. S10). That the timescale of protein complex assembly is nearly invariant to concentration over a broad range⁴³ is a unique feature of the KaiB–KaiC system, likely because the binding timescale is rate-limited by the KaiC ATPase cycle and the foldswitching of KaiB. This robustness of timing against fluctuating concentration would be difficult to achieve via other assembly control mechanisms (Fig. S11).

Outlook

Biomolecular signaling systems typically must maintain their function with high fidelity while interacting with numerous other components crowded within living cells and while subject to unpredictable fluctuations in their environment. These constraints equip networks of interacting biomolecules with unique robustness properties that may allow them to be harnessed to endow synthetic materials and systems with functionality, programmability, and autonomous reconfigurability. However, coupling biomolecular systems to synthetic materials to impart desired properties remains a grand challenge in active matter and biomaterials research^{24,46–49}. Here, we break new ground by using the KaiABC circadian clock as a prototypical example of a robust biomolecular signaling system. We demonstrate that this system can maintain its natural activity even when functionalized to act as a material crosslinker, and that it can then be used to autonomously regulate timed material self-assembly and oscillation. Specifically, we show that Kai proteins can assemble colloidal suspensions into networks of mesoscopic clusters at rates and efficiencies that are controlled by the phosphorylation state of KaiC. These molecular interactions translate to bulk changes in the sedimentation properties of the materials, visible by the naked eye. Moreover, our mathematical models show that the valency of the clock protein crosslinkers can be used as a switch to allow either sustained self-assembly or rapid dissolution of the material. In intermediate regimes of valency, this system drives oscillatory material properties.

This proof-of-concept opens the door to Kai-mediated scheduled crosslinking of a diversity of synthetic and natural materials, such as hydrogels, polymeric fluids, cellulose, and granular materials, to drive user-defined autonomous changes in material properties on a programmable schedule. Importantly, the timing of material self-assembly can not only be robustly programmed by Kai clock proteins, but that timing can be precisely tuned with the use of KaiC mutants that operate on cycles of different durations from ~15 to 158 h⁴⁰. The intrinsic temperature compensation property of KaiC would further ensure that the kinetics of assembly are robust against environmental fluctuations⁵⁰. Other accessory proteins, including SasA and CikA can be incorporated and functionalized to allow for material interactions peaking at other phases of the cycle²⁷.

These designs can potentially be used to create technologies such as dynamic filtration and sequestration devices, self-healing infrastructure, and programmable wound suturing. Beyond material crosslinking, the Kai system could be used as a synthetic scaffold to gate enzymatic activity to control the release of drugs or achieve metabolic channeling by enforcing spatial proximity between other entities. Beyond time-keeping, biological systems are capable of many information-processing tasks including thresholding, fold-change detection, and sign-sensitive filtering of input signals. Because these systems all function based on high molecular specificity, they represent a natural library of computational devices that can be coupled to non-biological systems to achieve autonomous control.

Methods

Protein preparation and characterization

Protein expression and purification. KaiA, KaiB, KaiC, pT KaiC (KaiC-AE; S431A, T432E), and pS KaiC (KaiC-EA; S431E, T432A) were recombinantly expressed and purified as previously described^{43,51}. For experiments other than the initial characterization by FP in Fig. 2C, wild-type (WT) KaiC carried an N-terminal FLAG epitope and was expressed using a SUMO tag following²⁷. Purified proteins were buffer-exchanged into Kai buffer containing: 10% glycerol, 150 mM NaCl, 20 mM Tris-HCl (pH 8.0), 5 mM MgCl₂, 0.5 mM EDTA (pH 8.0), 1 mM ATP (pH 8.0). Protein concentration was measured by Bradford Assay (Bio-Rad) using BSA as a standard.

Biotinylation of KaiB. KaiB stock (70 μM) was buffer-exchanged into labeling buffer (pH 8.0), containing 20 mM HEPES and 150 mM NaCl, using Zeba Spin Desalting Columns with 7KD MWCO (ThermoFisher). KaiB was functionalized with biotin using EZ-Link-Sulfo-NHS-LC-Biotin (ThermoFisher). The biotin reagent was added in 50× molar excess to KaiB, and the reaction was incubated at room temperature for 30 min. Unincorporated biotin was then removed using Zeba spin columns equilibrated in Kai buffer.

Pull-down assay of KaiBC complexes using b-KaiB as bait. Reactions with 6.5 μM KaiC (WT, pT, or pS) were mixed with 5.5 μM KaiB (55% b-KaiB, 45% unlabeled KaiB) in Kai buffer. The negative control did not contain b-KaiB (6.0 μM unlabeled KaiB). All reactions were incubated for 20 h at 30 °C to allow protein complex formation. b-KaiB and its binding partners were removed from solution by incubation with streptavidin-coated magnetic beads (Cytiva). To prepare the bead slurry, 20 μL of the resin stock was washed twice with 100 μL of Kai buffer. The resulting pellet was resuspended with 5 μL of the Kai protein reaction. The remaining 10 μL of each Kai protein reaction was saved as input samples. The reaction was incubated for 30 min at 22 °C with shaking at 950 rpm, after which the beads were magnetically pelleted. The resulting supernatant was transferred into a new tube. The beads were washed twice with 100 μL of Kai buffer and then boiled in SDS-PAGE sample buffer (reducing) at 98 °C for 5 min to elute the proteins from the beads. The eluate was transferred into a new tube. The input, supernatant, and eluate were analyzed by SDS-PAGE using 4–20% Criterion TGX gels (Bio-Rad) and stained using SYPRO Ruby (Invitrogen).

Fluorescence polarization. To characterize the tolerance of the standard oscillator reaction to b-KaiB, clock reactions were prepared by mixing together 1.5 μM KaiA, 3.5 μM KaiC, different ratios of KaiB and b-KaiB, and 0.2 μM FITC-labeled KaiB^{K25C} in Kai buffer, similar to the procedure used previously⁵². For each reaction, the total concentration of KaiB and b-KaiB was 3.5 μM. 30 μL of the reaction mixture was added to a black 384-well plate, which was sealed with low-autofluorescence polyolefin film (USA Scientific). The plate was loaded into a plate reader to measure FP with 485 nm excitation (20 nm bandpass) and 535 nm emission (25 nm bandpass) using a 510-nm dichroic filter. Measurements were taken every 15 min. Wells containing only Kai storage buffer were used as blanks. We performed the same FP assay to characterize protein function under colloid-linking conditions. For these experiments, we mixed together 5.5 μM KaiB (55% b-KaiB, 45% unlabeled KaiB), 6.5 μM KaiC (WT, pT, or pS), 2.2 μM KaiA, and 0.4 μM FITC-labeled KaiB^{K25C} in Kai buffer.

Characterization of phosphorylation state of KaiC in the colloidal system. KaiC phosphorylation in each sample was resolved by SDS-PAGE analysis using 10% Criterion Tris-HCl gels (Bio-Rad) run for 3 h at 125 V. The gels were stained with SYPRO Ruby (Invitrogen) and imaged using ChemiDoc (Bio-Rad). The ratio of phosphorylated KaiC to unphosphorylated KaiC was quantified by gel densitometry.

Clock-colloid experiments

Colloidal suspensions. We used streptavidin-coated Fluoresbrite YG 1.0-μm diameter polystyrene microspheres (Polysciences) as the colloids in all experiments which were stored suspended in water at 1.4% solids at 4 °C. Immediately prior to each experiment, the colloids were washed and resuspended to 3.7% solids in Kai reaction buffer as follows. 58 μL of the stock suspension was centrifuged in a low-retention microcentrifuge tube at 11500 × *g* for 5 min to pellet the colloids. The supernatant was immediately removed and replaced with 80 μL of Kai buffer, followed by vortexing to resuspend the colloids. This washing process was repeated two more times. Following the third spin down, the colloids were resuspended at 3.7% solids in Kai buffer. The suspension was mixed by vortexing and then further homogenized by sonication for 45 min at 4 °C.

To prepare Kai-colloid suspensions, we added 3.6 μM b-KaiB to the sonicated colloidal suspension, vortexed for ~3 s, and incubated at room temperature for 5 min to allow b-KaiB to coat the colloids. Next, we mixed in 2.9 μM unlabeled KaiB and 2.2 μM KaiA (for WT KaiC experiments) to create a master mix that we then divided into three tubes to which we added 6.5 μM of KaiC (WT, pS, or pT). We define $t = 0$ as the time of KaiC addition. The final colloid concentration was 1.26% solids ($\sim 4.0 \times 10^{-5}$ μM) in all cases.

Microscopy samples. Kai-colloid suspensions were flowed via capillary action into passivated sample chambers which were prepared as follows. Glass microscope slides and No. 1 coverslips were cleaned with methanol, rinsed with deionized water, and air dried. Three 22 mm × 3 mm flow channels were formed by fusing the slide and slip together with heated ~120-μm thick parafilm spacers to accommodate 8 μL of sample in each channel. To prevent non-specific binding of colloids and proteins to the chamber walls, we passivated the surfaces using BSA⁵³ as follows. We filled sample chambers with 10 mg/mL BSA in Kai buffer, incubated in a hydrated chamber at room temperature for 30 min, then flushed the BSA solution out with fresh Kai buffer. Sample chambers were then filled with the colloidal suspension, sealed with UV-curable adhesive, and placed on a 360° rotator at 30 °C. For each experiment, two replicates of each case were prepared and imaged immediately after one another.

Microscopy experiments. Colloidal suspensions were imaged using an Olympus IX73 epifluorescence microscope with a 40× 0.6 NA objective, 480/535-nm excitation/emission filters, and a Hamamatsu ORCA-Flash 2.8 CMOS camera. 1920 × 1440 square-pixel images of suspensions were captured 2–4 μm above the coverslip, in six equidistant regions around the horizontal center of sample chambers. Single images were captured sequentially for each sample in the three-lane chamber within a span of 5 min, for a total of 18 images in a 15 min period. This process was then immediately repeated for the replicate chamber. This set of 18 images was captured every ~3 h over a 28 h period. All data shown consists of 2–3 replicate experiments with vertical error bars representing standard error. Horizontal error bars indicate the variation in image acquisition times across replicates binned together into one data point (~15 min for most cases).

To construct confocal z-stacks shown in Figs. S2 and S5, we imaged samples using a Nikon AIR scanning confocal microscope with a 60× 1.4 NA oil-immersion objective. Colloids were imaged using a 488 nm laser with 488/595 nm excitation/emission filters. Stacks of 51 square images, with planar edge lengths of 512 pixels (210 μm), were constructed using a 0.2 μm z-step size, starting from the coverslip ($z = 0$) and going up to $z = 10$ μm.

Image post-processing and analysis. We analyzed images using three different approaches (see Figs. S7 and 3). All image post-processing and analyses were performed using custom-written Python codes^{54–56}. We first evaluated the distribution of pixel intensities across all images

for a given time point and condition, which we normalized to probability density distributions (Fig. S7D). To account for variations in image brightness across different images we subtracted from each pixel value the [mean–minimum] pixel value. We construct histograms using 5000 bins.

We also performed SIA analysis in Fourier space (Fig. S7E) and directly measured 2D cluster sizes in real space (Fig. S7F). For both analyses, we first binarized images by using local thresholding algorithms with a local block of 1051×1051 pixels⁵⁷, such that all pixel values were converted to 1 or 0. To measure cluster sizes, we identified each connected set of pixels above threshold as a cluster and count the number of pixels in each such region. By dividing the number of pixels within each 2D area by the maximum cross-sectional area of a colloid, we estimated the size of each cluster in terms of the minimum number of colloids it comprises. To quantify the distribution of cluster sizes we evaluated the cumulative distribution function of cluster sizes across all images for a given time point and condition (Fig. S7F and S8).

We used the same binarized images to perform SIA, which measures the correlation in intensity values $g(r)$ of each pair of pixels in a given image that are separated by a radial distance r ⁵⁸, and averages over all pairs with a given r . In practice, we generated $g(r)$ for each image by taking the fast Fourier transform of the image $F(I(r))$, multiplying by its complex conjugate, applying an inverse Fourier transform F^{-1} and normalizing by the squared intensity $[I(r)]^2$: $g(r) = [F^{-1}|F(I(r))|^2]/[I(r)]^2$. We generated a separate $g(r)$ curve for each image, and the data shown in Figs. 3–5 are the average and standard error of $g(r)$ across all images at a given time and condition. To quantify a characteristic lengthscale associated with the features (e.g., colloids, clusters) in a given image, we fitted the corresponding $g(r)$ to an exponential function, $g(r) = (1 - A)e^{-r/\xi} + A$, where A is a constant that accounts for non-zero asymptotes and ξ is the correlation length that estimates the average size of clusters in an image. To generate the experimental data shown in Figs. 3–5, we computed ξ for each image, averaged over all images for a given condition and time point, and normalized by the colloid diameter to quantify ξ in terms of the number of colloids it spans.

Sedimentation experiments. Sedimentation experiments were carried out in borosilicate glass capillaries with 1 mm \times 1 mm inner cross-section, 0.2 mm wall thickness and 11 mm length (Wale Apparatus, #8100-050), accommodating -10 μ L of aqueous sample. Capillaries are secured to a 10 mm \times 25 mm microscope slide with UV-curable adhesive, oriented such that each end extends -0.5 mm beyond the slide. The overhanging ends were then sanded to be flush with the slide. The colloidal suspensions, prepared as described above, were pipetted into the capillaries via capillary action. To seal the capillaries, glass coverslips (7 mm \times 22 mm) were adhered to the bottom and top openings using UV-curable adhesive. A second coat of UV-curable adhesive was added to the junctions between the chambers and coverslip to prevent sample evaporation and leakage.

The samples were mounted vertically against a white background in an enclosed space protected from light. To acquire time-lapse images of the colloidal suspensions undergoing sedimentation, the mounted capillaries were illuminated with a white light LED and 1024×1024 square-pixel images were captured every hour for 36 h using an iPhone 6s. The capillaries and lighting remain unperturbed for the entire 36-h acquisition.

Mathematical modeling and simulations

We simulated the dynamics of the experimental system using Brownian Dynamics implemented in C++⁵⁹, as described fully in SI. Our system consisted of 500 colloidal particles of diameter $\sigma = 1 \mu\text{m}$, confined to a two-dimensional box with edge length 50 μm and periodic boundary conditions. The colloids occupied a static area fraction of

16%, set to match experimental conditions by evaluating the fraction of pixels above threshold in binarized experimental images. At the beginning of each simulation, all colloids were separate particles undergoing Brownian diffusion in 2D. When the surfaces of two colloids come within a distance $l = 10 \text{ nm}$ of each other (the approximate size of a KaiBC complex⁴⁵), they have a non-zero probability of linking together. We simulated three cases that correspond to our experimental studies: (1) Permanent crosslinking, where, once formed, bonds between colloidal particles are permanent; (2) No crosslinking, where bonds never form between colloidal particles regardless of their proximity; and (3) Oscillatory crosslinking, where bond formation and dissolution follow the oscillatory complexing of KaiB and KaiC. SI Table S1 provides all simulation parameters, their relation to experimental values, and rationale for their choice.

For cases (1) and (3), when a pair of particles are within a center-to-center distance of $r_0 = \sigma + l$, they can become crosslinked with a certain probability. This attachment probability at simulation time t is $p_a = p_0 \cos^2(\pi t/T)$, where $T = 24 \text{ h}$ represents the crosslinker oscillation period. The probability amplitude p_0 is a phenomenological parameter determined from the FP data for pS KaiC (see Fig. 3F). In cases where the particles can unlink, we implement a detachment probability, $p_d = p_0^n \sin^2(\pi t/T)$, where n is the number of bonds (KaiABC crosslinkers) connecting the particle pair under consideration. At the beginning of the simulation, the system has a maximum probability of attachment and a minimum detachment probability to replicate the experimental schedule of the KaiB–KaiC interaction. We ran simulations for 69120τ , corresponding to 48 h of experimental time (see SI Movies S1–S5 and Table S1), and show averages over five runs in the results presented in the paper.

Statistics and reproducibility

No statistical method was used to predetermine sample size. No data were excluded from the analyses.

Reporting summary

Further information on research design is available in the Nature Portfolio Reporting Summary linked to this article.

Data availability

The data generated in this study are provided in the Source Data file and have been deposited in the Zenodo database under accession code <https://doi.org/10.5281/zenodo.14451964>. Source data are provided with this paper.

Code availability

The codes used for all simulations have been deposited in the Zenodo database under accession code <https://doi.org/10.5281/zenodo.14451964>. Analysis codes are provided on GitHub (see refs. 54–56).

References

- Chen, Y., Yeh, C. J., Qi, Y., Long, R. & Creton, C. From force-responsive molecules to quantifying and mapping stresses in soft materials. *Sci. Adv.* **6**, eaaz5093 (2020).
- Jahnke, K. et al. Engineering light-responsive contractile actomyosin networks with DNA nanotechnology. *Adv. Biosyst.* **4**, 2000102 (2020).
- Kučera, O., Gaillard, J., Guérin, C., Théry, M. & Blanchoin, L. Actin–microtubule dynamic composite forms responsive active matter with memory. *Proc. Natl. Acad. Sci. USA* **119**, e2209522119 (2022).
- Sun, H., Kabb, C. P., Sims, M. B. & Sumerlin, B. S. Architecture-transformable polymers: reshaping the future of stimuli-responsive polymers. *Prog. Polym. Sci.* **89**, 61–75 (2019).
- Zhu, J. et al. Light-responsive colloidal crystals engineered with DNA. *Adv. Mater.* **32**, 1906600 (2020).
- Xu, W. et al. Metal-organic frameworks enhance biomimetic cascade catalysis for biosensing. *Adv. Mater.* **33**, 2005172 (2021).

7. Kim, Y. S., Tamate, R., Akimoto, A. M. & Yoshida, R. Recent developments in self-oscillating polymeric systems as smart materials: from polymers to bulk hydrogels. *Mater. Horiz.* **4**, 38–54 (2017).
8. Li, J. et al. Recent advances in flexible self-oscillating actuators. *eScience* **4**, 100250 (2024).
9. Hua, M. et al. Swaying gel: chemo-mechanical self-oscillation based on dynamic buckling. *Matter* **4**, 1029–1041 (2021).
10. Ali, N., Nand, S., Kiran, A., Mishra, M. & Mehandia, V. Oscillating rheological behavior of Turbatrix aceti nematodes. *Phys. Fluids* **35**, 011906 (2023).
11. Shao, Q., Zhang, S., Hu, Z. & Zhou, Y. Multimode self-oscillating vesicle transformers. *Angew. Chem. Int. Ed.* **59**, 17125–17129 (2020).
12. Liu, A. P. & Fletcher, D. A. Biology under construction: in vitro reconstitution of cellular function. *Nat. Rev. Mol. Cell Biol.* **10**, 644–650 (2009).
13. Zieske, K. & Schwille, P. Reconstitution of self-organizing protein gradients as spatial cues in cell-free systems. *eLife* **3**, e03949 (2014).
14. Nakajima, M. et al. Reconstitution of circadian oscillation of cyanobacterial KaiC phosphorylation in vitro. *Science* **308**, 414–415 (2005).
15. Das, M., F. Schmidt, C. & Murrell, M. Introduction to active matter. *Soft Matter* **16**, 7185–7190 (2020).
16. Majidi, C. Soft-matter engineering for soft robotics. *Adv. Mater. Technol.* **4**, 1800477 (2019).
17. Vernerey, F. J. et al. Biological active matter aggregates: inspiration for smart colloidal materials. *Adv. Colloid Interface Sci.* **263**, 38–51 (2019).
18. Fan, X. & Walther, A. 1D Colloidal chains: recent progress from formation to emergent properties and applications. *Chem. Soc. Rev.* **51**, 4023–4074 (2022).
19. Needleman, D. & Dogic, Z. Active matter at the interface between materials science and cell biology. *Nat. Rev. Mater.* **2**, 1–14 (2017).
20. Burla, F., Mulla, Y., Vos, B. E., Aufderhorst-Roberts, A. & Koenderink, G. H. From mechanical resilience to active material properties in biopolymer networks. *Nat. Rev. Phys.* **1**, 249–263 (2019).
21. Liu, S., Shankar, S., Marchetti, M. C. & Wu, Y. Viscoelastic control of spatiotemporal order in bacterial active matter. *Nature* **590**, 80–84 (2021).
22. Zhang, R. et al. Spatiotemporal control of liquid crystal structure and dynamics through activity patterning. *Nat. Mater.* **20**, 875–882 (2021).
23. Xu, H., Huang, Y., Zhang, R. & Wu, Y. Autonomous waves and global motion modes in living active solids. *Nat. Phys.* 1–6. <https://doi.org/10.1038/s41567-022-01836-0> (2022).
24. Liu, A. P. et al. The living interface between synthetic biology and biomaterial design. *Nat. Mater.* **21**, 390–397 (2022).
25. Srubar, W. V. Engineered living materials: taxonomies and emerging trends. *Trends Biotechnol.* **39**, 574–583 (2021).
26. Zhang, R., Mozaffari, A. & de Pablo, J. J. Autonomous materials systems from active liquid crystals. *Nat. Rev. Mater.* **6**, 437–453 (2021).
27. Chavan, A. G. et al. Reconstitution of an intact clock reveals mechanisms of circadian timekeeping. *Science* **374**, eabd4453 (2021).
28. LiWang, A. et al. Reconstitution of an intact clock reveals mechanisms of circadian timekeeping. *Biophys. J.* **121**, 331a (2022).
29. Mori, T. et al. Revealing circadian mechanisms of integration and resilience by visualizing clock proteins working in real time. *Nat. Commun.* **9**, 3245 (2018).
30. Rust, M. J., Markson, J. S., Lane, W. S., Fisher, D. S. & O’Shea, E. K. Ordered phosphorylation governs oscillation of a three-protein circadian clock. *Science* **318**, 809–812 (2007).
31. Oyama, K., Azai, C., Nakamura, K., Tanaka, S. & Terauchi, K. Conversion between two conformational states of KaiC is induced by ATP hydrolysis as a trigger for cyanobacterial circadian oscillation. *Sci. Rep.* **6**, 32443 (2016).
32. Sasai, M. Mechanism of autonomous synchronization of the circadian KaiABC rhythm. *Sci. Rep.* **11**, 4713 (2021).
33. Kawamoto, N., Ito, H., Tokuda, I. T. & Iwasaki, H. Damped circadian oscillation in the absence of KaiA in *Synechococcus*. *Nat. Commun.* **11**, 2242 (2020).
34. Dong, P. et al. A dynamic interaction process between KaiA and KaiC is critical to the cyanobacterial circadian oscillator. *Sci. Rep.* **6**, 25129 (2016).
35. Chang, Y.-G., Tseng, R., Kuo, N.-W. & LiWang, A. Rhythmic ring–ring stacking drives the circadian oscillator clockwise. *Proc. Natl. Acad. Sci. USA* **109**, 16847–16851 (2012).
36. Tseng, R. et al. Structural basis of the day–night transition in a bacterial circadian clock. *Science* **355**, 1174–1180 (2017).
37. Snijder, J. et al. Insight into cyanobacterial circadian timing from structural details of the KaiB–KaiC interaction. *Proc. Natl. Acad. Sci. USA* **111**, 1379–1384 (2014).
38. Swan, J. A., Golden, S. S., LiWang, A. & Partch, C. L. Structure, function, and mechanism of the core circadian clock in cyanobacteria. *J. Biol. Chem.* **293**, 5026–5034 (2018).
39. Chang, Y.-G. et al. A protein fold switch joins the circadian oscillator to clock output in cyanobacteria. *Science* **349**, 324–328 (2015).
40. Ito-Miwa, K., Furuie, Y., Akiyama, S. & Kondo, T. Tuning the circadian period of cyanobacteria up to 6.6 days by the single amino acid substitutions in KaiC. *Proc. Natl. Acad. Sci. USA* **117**, 20926–20931 (2020).
41. Nishiwaki, T. et al. A sequential program of dual phosphorylation of KaiC as a basis for circadian rhythm in cyanobacteria. *EMBO J.* **26**, 4029–4037 (2007).
42. Terauchi, K. et al. ATPase activity of KaiC determines the basic timing for circadian clock of cyanobacteria. *Proc. Natl. Acad. Sci. USA* **104**, 16377–16381 (2007).
43. Phong, C., Markson, J. S., Wilhoite, C. M. & Rust, M. J. Robust and tunable circadian rhythms from differentially sensitive catalytic domains. *Proc. Natl. Acad. Sci. USA* **110**, 1124–1129 (2013).
44. Cohen, S. E. & Golden, S. S. Circadian rhythms in cyanobacteria. *Microbiol. Mol. Biol. Rev.* **79**, 373–385 (2015).
45. Snijder, J. et al. Structures of the cyanobacterial circadian oscillator frozen in a fully assembled state. *Science* **355**, 1181–1184 (2017).
46. Nguyen, P. Q., Courchesne, N.-M. D., Duraj-Thatte, A., Praveschotinunt, P. & Joshi, N. S. Engineered living materials: prospects and challenges for using biological systems to direct the assembly of smart materials. *Adv. Mater.* **30**, 1704847 (2018).
47. Tang, T.-C. et al. Materials design by synthetic biology. *Nat. Rev. Mater.* **6**, 332–350 (2021).
48. Brooks, S. M. & Alper, H. S. Applications, challenges, and needs for employing synthetic biology beyond the lab. *Nat. Commun.* **12**, 1390 (2021).
49. Li, J. et al. Abiotic–biological hybrid systems for CO₂ conversion to value-added chemicals and fuels. *Trans. Tianjin Univ.* **26**, 237–247 (2020).
50. Murayama, Y. et al. Low temperature nullifies the circadian clock in cyanobacteria through Hopf bifurcation. *Proc. Natl. Acad. Sci. USA* **114**, 5641–5646 (2017).
51. Lin, J., Chew, J., Chockanathan, U. & Rust, M. J. Mixtures of opposing phosphorylations within hexamers precisely time feedback in the cyanobacterial circadian clock. *Proc. Natl. Acad. Sci. USA* **111**, E3937–E3945 (2014).
52. Leypunskiy, E. et al. The cyanobacterial circadian clock follows midday in vivo and in vitro. *eLife* **6**, e23539 (2017).
53. Ma, G. J., Ferhan, A. R., Jackman, J. A. & Cho, N.-J. Conformational flexibility of fatty acid-free bovine serum albumin proteins enables superior antifouling coatings. *Commun. Mater.* **1**, 1–11 (2020).

54. Leech, G. Best SIA image analysis. <https://github.com/gregorleech/best-SIA-image-analysis> (2022).
55. Leech, G. Best cluster analysis. <https://github.com/gregorleech/best-cluster-analysis> (2022).
56. McGorty, R. Image autocorrelation. <https://github.com/rmcgorty/ImageAutocorrelation> (2021).
57. van der Walt, S. et al. scikit-image: image processing in Python. *PeerJ* **2**, e453 (2014).
58. Robertson, C. & George, S. C. Theory and practical recommendations for autocorrelation-based image correlation spectroscopy. *J. Biomed. Opt.* **17**, 080801 (2012).
59. Melcher, L. et al. Sustained order–disorder transitions in a model colloidal system driven by rhythmic crosslinking. *Soft Matter* **18**, 2920–2927 (2022).
60. Pattanayek, R. & Egli, M. Crystal structure of circadian clock protein KaiB from *S. Elongatus*. RCSB Protein Data Bank. <https://doi.org/10.2210/pdb4kso/pdb> (2013).
61. Villarreal, S. A. et al. CryoEM and molecular dynamics of the circadian KaiB–KaiC complex indicates that KaiB monomers interact with KaiC and block ATP binding clefts. *J. Mol. Biol.* **425**, 3311–3324 (2013).

Acknowledgements

We thank Jeffrey Wang, Eliana Petreikis, and Tia Peterson for their work on the design of the system; and Katarina Matic, Maya Hendija, and Juexin Marfai for assistance with control experiments. We thank Megan Valentine, Ryan McGorty, and Jonathan Michel for insightful discussions. This work was funded by a WM Keck Foundation Research grant awarded to R.M.R.A., J.L.R., M.J.R., and M.D.; NSF DMREF grants: DMR-2119663 to R.M.R.A., NSF DMR-2118403 to J.L.R., NSF DMR-2118424 to M.J.R., NSF DMR-2118449 to M.D.; and NIH R01 GM107369 to M.J.R.

Author contributions

Conceptualization: J.L.R., M.D., M.J.R., R.M.R.A. Methodology: J.L.R., M.D., M.J.R., R.M.R.A., G.L. Investigation: G.L., L.M., M.C., S.J., M.N., L.B., J.K., S.J.K., S.B., L.F., M.J.R., M.D., J.L.R., R.M.R.A. Visualization: G.L., M.C., L.M., M.N., R.M.R.A. Supervision: J.L.R., M.D., M.J.R., R.M.R.A. Writing—original draft: G.L., L.M., M.J.R., M.D., R.M.R.A. Writing—review & editing: G.L., M.C., J.L.R., M.D., M.J.R., R.M.R.A.

Competing interests

The authors declare no competing interests.

Additional information

Supplementary information The online version contains supplementary material available at <https://doi.org/10.1038/s41467-024-55645-5>.

Correspondence and requests for materials should be addressed to Rae M. Robertson-Anderson.

Peer review information *Nature Communications* thanks the anonymous reviewers for their contribution to the peer review of this work. A peer review file is available.

Reprints and permissions information is available at <http://www.nature.com/reprints>

Publisher's note Springer Nature remains neutral with regard to jurisdictional claims in published maps and institutional affiliations.

Open Access This article is licensed under a Creative Commons Attribution-NonCommercial-NoDerivatives 4.0 International License, which permits any non-commercial use, sharing, distribution and reproduction in any medium or format, as long as you give appropriate credit to the original author(s) and the source, provide a link to the Creative Commons licence, and indicate if you modified the licensed material. You do not have permission under this licence to share adapted material derived from this article or parts of it. The images or other third party material in this article are included in the article's Creative Commons licence, unless indicated otherwise in a credit line to the material. If material is not included in the article's Creative Commons licence and your intended use is not permitted by statutory regulation or exceeds the permitted use, you will need to obtain permission directly from the copyright holder. To view a copy of this licence, visit <http://creativecommons.org/licenses/by-nc-nd/4.0/>.

© The Author(s) 2024